nature electronics

Article

https://doi.org/10.1038/s41928-023-01068-x

A conformable phased-array ultrasound patch for bladder volume monitoring

Received: 19 January 2023

Accepted: 12 October 2023

Published online: 16 November 2023

Check for updates

Lin Zhang[1,8], Colin Marcus[1,2,8], Dabin Lin[3,8], David Mejorado[1], Scott Joseph Schoen Jr[4], Theodore T. Pierce[4], Viksit Kumar[4], Sara V. Fernandez[1,5], David Hunt[4], Qian Li[4], Ikra Iftekhar Shuvo[1], David Sadat[1], Wenya Du[1], Hannah Edenbaum[4], Li Jin[6], Weiguo Liu[3], Yonina C. Eldar[7], Fei Li[6], Anantha P. Chandrakasan[2], Anthony E. Samir[4] & Canan Dagdeviren[1]

Ultrasound can be used to image soft tissues in vivo for the early diagnosis and monitoring of disease progression. However, conventional ultrasound probes are rigid, have a narrow field of view and are operator dependent. Conformable transducers have been proposed, but they lack efficient element localization and effective spatial resolution during mechanical deformations. Here we report a conformable ultrasound bladder patch that is based on multiple phased arrays embedded in a stretchable substrate and can provide mechanically robust, conformable and in vivo volumetric organ monitoring. The phased arrays use Sm/La-doped $Pb(Mg_{1/3}Nb_{2/3})O_3$–$PbTiO_3$ ceramics as the piezoelectric material, which offers superior properties (d_{33} = 1,000 pC N^{-1}, ε_r = 7,500 and k_{33} = 0.77) than conventional piezoelectric ceramics. We use the conformable ultrasound patch in a pilot clinical study of bladder monitoring. Bladder volume estimation with the patch is comparable (relative errors of 3.2 ± 6.4% and 10.8 ± 8.2% with and without ultrasound gel, respectively) to that obtained using standard clinical ultrasound equipment, and not requiring manual translation or rotation by an operator.

Advances in material fabrication technology and mechanical engineering have led to the development of high-performance piezoelectric systems in conformable formats[1–5]. Such piezoelectric conformable electronics can exhibit real-time and continuous signal monitoring and decoding for use in various biomedical and healthcare applications, including the monitoring of skin modulus[6,7], heart motion[8,9], facial motion[10,11], gastrointestinal motility[12], tactile stimuli[13], blood pressure[14,15] and blood flow[16]. Such technology can also be used to create piezoelectric ultrasound transducers that can provide insight into deep tissues and curvy organs through quantitative imaging, broadening our understanding of soft-tissue disorders.

Ultrasound is widely used in clinical practice because it is safe, non-invasive, non-ionizing, low cost and provides real-time imaging, monitoring and therapy. Replacing rigid transducers with conformable ultrasound transducer arrays can allow image acquisition on curved body parts, improve image quality and enable functions such as long-term monitoring and therapy[15–28]. However, it is challenging for current conformable piezoelectric ultrasonic arrays (Supplementary Note 1 and Supplementary Table 1) to simultaneously achieve high ultrasound image quality and mechanical stretchability due to the unpredictable change in the pitch of elements when an intrinsically stretchy surface is deformed (Supplementary Fig. 1a). Localizing the relative

[1]Media Lab, Massachusetts Institute of Technology, Cambridge, MA, USA. [2]Department of Electrical Engineering and Computer Science, Massachusetts Institute of Technology, Cambridge, MA, USA. [3]School of Opto-electronical Engineering, Xi'an Technological University, Xi'an, China. [4]Center for Ultrasound Research & Translation, Department of Radiology, Massachusetts General Hospital, Boston, MA, USA. [5]Department of Materials Science and Engineering, Massachusetts Institute of Technology, Cambridge, MA, USA. [6]Electronic Materials Research Laboratory, Key Laboratory of the Ministry of Education, School of Electronic Science and Engineering, Xi'an Jiaotong University, Xi'an, China. [7]Faculty of Math and Computer Science, Weizmann Institute of Science, Rehovot, Israel. [8]These authors contributed equally: Lin Zhang, Colin Marcus, Dabin Lin. e-mail: canand@media.mit.edu

positions of transducer elements requires the use of computationally complex compensation algorithms, optical fibres or cameras. Stretchability between elements also requires a larger pitch (usually >0.5 mm), which necessitates the use of low working frequencies to avoid grating lobe artifacts[28–31]. Conventional ultrasound transducers also require the application of pressure to achieve sufficient acoustic contact for imaging when placed on curved body surfaces. Therefore, an engineering approach is necessary to create conformable ultrasound devices that can achieve high spatial resolution, operate at higher, more diagnostically useful ultrasound frequencies and image over a broad field of view (FOV), particularly in the shallow near-field region.

The active piezoelectric material has a vital role in the performance of ultrasound transducers[32]. The majority of conformable ultrasound devices use commercial lead zirconate titanate (PZT) (Supplementary Table 1)[15–22,25,28]. Compared with traditional PZT-5H ceramic with relatively low piezoelectric properties (d_{33} < 700 pC N^{-1}, k_{33} < 0.6), $Pb(Mg_{1/3}Nb_{2/3})O_3$–$PbTiO_3$ (PMN-PT) ceramics doped with single rare-earth elements (La^{3+}, Sm^{3+}, Pr^{3+}, Yb^{3+} and Eu^{3+}) have attracted the interest of researchers due to their ultrahigh longitudinal piezoelectric coefficient and electromechanical coupling coefficients (Supplementary Table 3)[33–35]. Among reported rare-earth-doped ceramics, Sm-doped PMN-PT has the highest piezoelectric coefficient of the ferroelectric ceramics[34]. Rare-earth-doped PMN-PT-based transducers have been developed for piezoelectric transducer design[36,37], but rare-earth-doped PMN-PT ceramics have not been previously used to make ultrasound transducers for conformable ultrasound devices.

Interest in using ultrasound technology for monitoring the urinary bladder through the lower abdomen has led to various wearable or portable ultrasound devices being proposed (Supplementary Note 2 and Supplementary Table 2)[38–44]. However, most of these devices use limited numbers of elements to detect anterior–posterior organ dimension (A mode), resulting in imprecise volume estimation, difficulty with positioning the transducer and a limited view of the target organ. In addition, most portable systems still have a rigid, planar configuration, resulting in poor contact over curved body surfaces. For handheld probes, although they can obtain real-time bladder images, it is still required to rotate in two orientations (transverse and sagittal planes) to achieve a comprehensive view of the bladder (Fig. 1a). Despite high levels of training and experience, operator-to-operator measurement variability remains problematic. For these reasons, a conformable ultrasound device that can seamlessly conform to the body and decode the signals from both skin surface and deep tissue is desirable.

In this Article, we report a conformable ultrasound bladder patch (cUSB-Patch) that is mechanically adaptive and can provide the real-time in vivo monitoring of bladder volume (Fig. 1b,c and Supplementary Fig. 2). We develop a Sm/La-doped PMN-PT ceramic material with high piezoelectric properties (d_{33} = 1,000 pC N^{-1}, ε_r = 7,500 and k_{33} = 0.77) and use it to fabricate a 64-element phased-array transducer with an operational frequency of 2–5 MHz (Fig. 1g–j). The patch offers mechanically adaptive and real-time in vivo monitoring of bladder volume (Fig. 1d–f). To avoid the requirement for manual rotation, the cUSB-Patch can simultaneously obtain images in two orientations. The device can image the urinary bladder at a depth up to 15 cm with an axial resolution of less than 0.6 mm. Theoretical and in vitro experimental studies establish that the cUSB-Patch with five such arrays can provide accurate and reproducible imaging on different phantoms (planar and curved), with and without an ultrasound gel.

In a pilot clinical study, the cUSB-Patch centre transducer is shown to reliably locate the initial centre position of the bladder, whereas its five arrays image the bladder from multiple angles, enabling real-time imaging and measurement without the need for transducer motion or rotation. The cUSB-Patch can image other deep tissues without modification, and the architecture supports imaging shallower tissues by a simple adjustment of design parameters. Candidate clinical applications include the diagnosis and quantification of acute urinary retention, long-term monitoring of at-risk patients and an adjunct tool for paraplegic patients who could benefit from automatic and accurate bladder volume measurements. The use of a stretchable substrate with an elastic modulus comparable with the human epidermis provides conformable and seamless adhesion to the human body as well as an acoustically thin layer, allowing operation without the uncomfortable ultrasound gel frequently used in ultrasound imaging.

cUSB-Patch design for large-area imaging

Recent stretchable devices have used an island–bridge design to connect elements by serpentine electrodes (Supplementary Fig. 1, strategy I), but these face obstacles to large and precise imaging (Supplementary Note 1 and Supplementary Table 1)[16,20]. We instead use a multi-phased-array design (Supplementary Fig. 1, strategy II), which allows the technology to be integrated into a wearable format and provides a spatiotemporally accurate image reconstruction technique on a larger FOV for monitoring deeper body structures. In this approach, adjacent elements are merged closer to consolidate them in the form of phased arrays to achieve a balance between the ultrasound imaging resolution and mechanical stretchability. The phased array can be either a one-dimensional (1D) array or two-dimensional (2D) matrix array, with the aperture designed to achieve a larger FOV and cover the area between adjacent arrays. The design exhibits both local rigidity and global malleability, maintaining the imaging performance of the phased arrays and simultaneously allowing extensive surface-area coverage and mechanical deformation. The final image reconstruction is facilitated by the partial overlap between images from each phased array. Using strategy II, we recently reported a nature-inspired honeycomb patch in junction with a 1D phased array, which offered real-time, user-friendly and continuous monitoring of the curved breast tissue for early breast cancer screening[26,45].

As a proof of concept, the cUSB-Patch is designed for real-time bladder volume monitoring, an assessment that requires large-area continuous monitoring with high resolution, using novel Sm/La-PMN-PT ceramics. As shown in Fig. 1d–f and Supplementary Fig. 2, the cUSB-Patch constitutes a set of five 1D phased arrays: three arrays positioned in the transverse (horizontal) plane with a 5 cm array-to-array pitch and two arrays in the sagittal (vertical) direction with the same pitch. All the transducers in the transverse plane are oriented in the same direction, whereas the transducers in the sagittal plane are rotated 90° away from the centre array. Each array acquires a 2D slice of the tissue volume, with the slice width approximately equal to the array width. The imaging planes of several arrays can be combined to produce a unified image with improved FOV and resolution, especially close to the surface. Assuming the beam steering angle is greater than 30°, three arrays can cover a greater area than a conventional commercially available curved C5-2v or C1-6-D convex probe (Supplementary Fig. 2b). According to the patch design (Supplementary Fig. 3), the mould for the substrate consists of five elevated platforms with dimensions of 20.0 mm × 20.0 mm × 4.0 mm, which matches the size of each array. The thin layer of biocompatible silicone rubber (Ecoflex 00-30, Smooth-On) on top of the matching layer, prepared by dip coating, has two functions: one is to hold each array and the other is to provide acoustic coupling between the transducer and the target surface, which minimizes the need for the ultrasound gel. The overall thickness of the patch is less than 4.5 mm, but it is thicker than many Ecoflex-based electronic skins (<2 mm)[24,28,46], allowing for embedding the entire array and still achieving enough stretchability and stress recovery from mechanical deformation. When the patch is subjected to twisting, bending and lamination onto the surfaces of a curved phantom (Supplementary Fig. 4 and Supplementary Video 1), the relative position of elements per array remains stable, guaranteeing a consistent ultrasound beamforming from each array and operator independence because it does not necessitate manually applied pressure or scanning. In addition, when applied on the subject, the patch showed robust mechanical performance during bending with connected cables and when attaching and detaching

https://doi.org/10.1038/s41928-023-01068-x

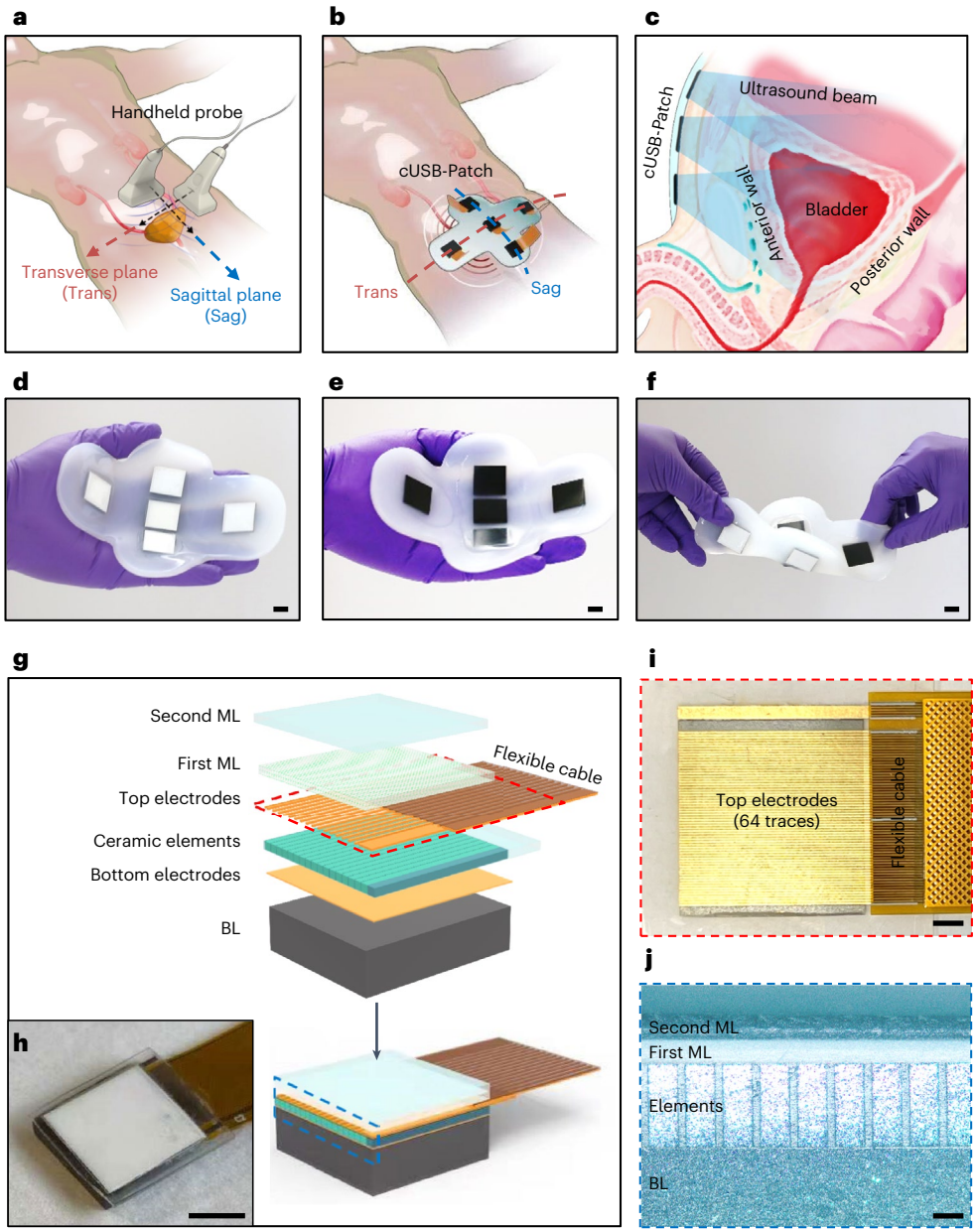

Fig. 1 | Overview of the phased array and cUSB-Patch. a, Schematic of the operation of a handheld probe on the human's lower abdomen for bladder imaging. To obtain a comprehensive view of the bladder in standard clinical practice, the handheld probe has to image in two orientations (transverse plane and sagittal plane) by rotating the ultrasound probe. **b**, Schematic of the cUSB-Patch on the human's lower abdomen for bladder imaging. To avoid the requirement for manual rotation, the cUSB-Patch can simultaneously obtain the images in two orientations. **c**, Schematic of a cross-sectional view of the cUSB-Patch on the lower abdomen. The phased arrays can locate the anterior and posterior walls of the bladder and cover the entire FOV of the bladder using multiple ultrasound beams. **d**–**f**, Natural and flexible form factor of the cUSB-Patch: on hand with the view of the matching layer's side (**d**), on hand with the view of the backing layer's side (**e**) and the image of the cUSB-Patch under twisting (**f**). **g**, Schematic of a single, ultrasound phased array with the key components labelled. The 1D linear high-performance piezoelectric elements are embedded in the epoxy matrix with a shared bottom electrode and independent top electrodes. A customized flex PCB cable (fabricated by PCBWay) is bonded with the electrodes. The backing layer (BL) and two matching layers (MLs) are bonded on the bottom and top sides, respectively. **h**, Optical image of a single phased array with the flexible cable. **i**, Optical image of the top view of the array with electrodes. The top electrode (64 traces) is well aligned with traces on the flexible cable. **j**, Optical image of the cross-section of the array, including diced La/Sm-PMN-PT ceramic elements with filled epoxy, a backing layer and two matching layers. Scale bars, 1 cm (**d**–**f**, **h**); 2 mm (**i**); 200 µm (**j**).

several times on the subject's lower abdomen (Supplementary Fig. 4 and Supplementary Video 2).

Piezoelectric performance of Sm/La-doped PMN-PT ceramics

In this work, PMN-PT ceramics doped with two rare-earth elements Sm and La (0.5–1.0 mol%) (termed Sm/La-PMN-PT) were synthesized using a high-temperature solid-state process with a hot-pressing technology (Methods). The selection of La as the second doping element is motivated by the discovery that the width of the micro–macro polar transition range in PMN-0.15PT ceramics increased after La modification, resulting in large electromechanical responses over a broader temperature range[47]. To achieve both high piezoelectric properties and a comprehensive range of temperature stability, especially for compositions

https://doi.org/10.1038/s41928-023-01068-x

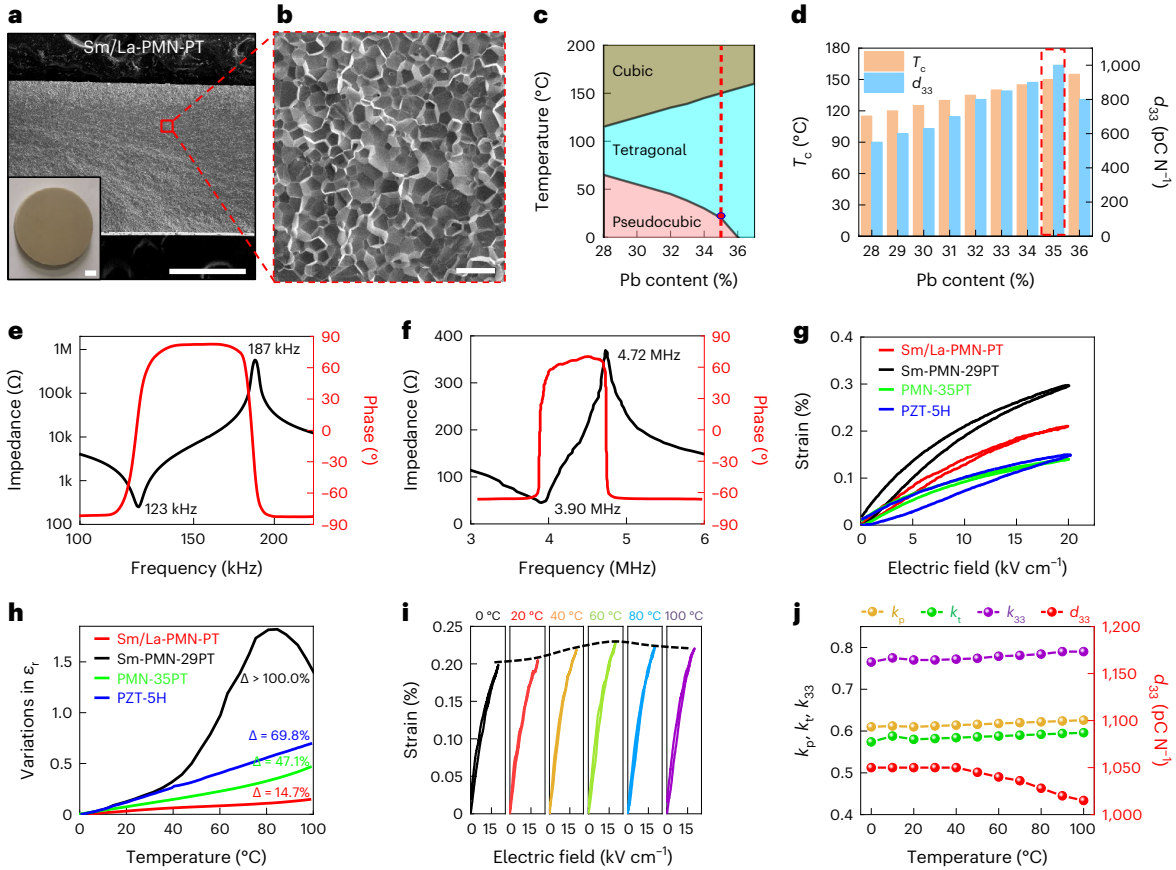

Fig. 2 | Characterization of morphological, piezoelectric and dielectric properties of Sm/La-PMN-*x*PT ceramics. a, Scanning electron microscopy (SEM) image of the cross-section of Sm/La-PMN-PT (Sm = La = 0.75%) ceramics. The inset shows the optical photograph of the ceramic disc with a high density of 7.92 g cm^{-3}. **b**, Zoomed-in SEM image of the ceramic grains. The red dashed line indicates the zoomed-in area marked in **a**. The selected SEM images are representative of the cross-section observation of five different specimens with the same doping amount and composition. **c**, Phase diagram of Sm/La-PMN-*x*PT. The red dashed line indicates the composition (x = 35%) selected in this work. **d**, Curie temperature T_c and piezoelectric coefficient d_{33} of Sm/La-PMN-*x*PT (x = 28–36). The composition with x = 35 (red dashed line) shows the best performance and was selected for transducer fabrication in this study. **e**, Frequency dependence of impedance and phase for a longitudinal bar (2 mm × 2 mm × 8 mm). **f**, Frequency dependence of impedance and phase for a flat plate (12 mm × 12 mm × 1 mm). **g**, Comparison of electric-field-induced strain of Sm/La-PMN-PT (Sm = La = 0.75%), Sm-PMN-29PT, PMN-35PT and PZT-5H ceramics, measured at 1 Hz at room temperature. **h**, Temperature dependence of the variation in relative dielectric constant (ε_r) for Sm/La-PMN-35PT, Sm-PMN-29PT, PMN-35PT and PZT-5H ceramics. **i**, Electric-field-induced strain behaviour of the Sm/La-PMN-PT (Sm = La = 0.75%) ceramic at selected temperatures: 0, 20, 40, 60, 80 and 100 °C. The black dashed line indicates the variation (15%) in the maximum strain value with temperature. **j**, Temperature dependence of the piezoelectric coefficient d_{33} and electromechanical coupling factors k_p, k_t and k_{33} for Sm/La-PMN-PT (Sm = La = 0.75%) ceramics. Scale bars, 0.5 cm (**a**); 20 μm (**b**).

near the morphotropic phase boundary[48], Sm/La-PMN-*x*PT ceramics with different contents of PT (x = 28–36) and Sm/La doping (0.50%, 0.75% and 1.00%) were systematically investigated (Supplementary Note 3). As shown in Supplementary Fig. 5, and with the micropores and grain size also playing important roles in shaping the properties of ceramics, the enhanced piezoelectric performance is ascribed to the dense and uniform microstructure (Fig. 2a,b). Due to La modifications, Sm/La-PMN-PT (Sm = La = 0.75%) ceramics exhibit well-developed density (7.92 g cm^{-3}), fine-grain microstructures, homogeneous element distribution (Supplementary Fig. 6) and the best performance compared with other doping amounts (Supplementary Table 3), which would benefit device performance for different applications such as actuators and piezoelectric transducers. According to the phase diagram shown in Fig. 2c, the pseudocubic–tetragonal phase boundary of the PMN-PT system is shifted to a lower PT content by doping rare-earth elements, and the maximum value is observed on the tetragonal side of the morphotropic-phase-boundary region. For this reason, the Curie temperature (T_c) value increases as the Pb content increases, whereas the d_{33} value first increases and reaches the peak value of 1,000 pC N^{-1} at room temperature at x = 35, and then decreases (Fig. 2d). In addition, around the Pb content of 35%, the relative dielectric permittivity and electromechanical coupling factors (k_p and k_t) increase to 7,500, 0.62 and 0.58, respectively, whereas the dielectric loss (tanδ) value remains relatively low (<0.02) (Supplementary Fig. 7). Additionally, Fig. 2e,f demonstrates the resonance and antiresonance frequency features of the impedance and phase in the longitudinal bar and flat plate, respectively, validating both enhanced electromechanical and piezoelectric properties as expressed by larger d_{33}. The electromechanical coupling factors (k_{33} = 0.77 and k_t = 0.58) are calculated from these obtained data, indicating substantially larger electromechanical coupling factors compared with PZT-5H and undoped PMN-PT ceramics (Supplementary Table 3). To illustrate the comparative piezoelectric response, electric-field-induced strain measurement with different ceramics was carried out (Fig. 2g). The Sm/La-PMN-PT (Sm = La = 0.75%) ceramic exhibited a larger strain (21%) than those of the widely used PMN-35PT and PZT-5H ceramics[34].

Comparing between the four representative ceramics, the results listed in Supplementary Table 3 indicate that the dielectric and piezoelectric performances of the Sm/La-PMN-PT (Sm = La = 0.75%) ceramic are better than both commercial PZT-5H and PMN-32PT ceramics but slightly lower than the performance of the state-of-the-art Sm-PMN-29PT (Sm = 2.5%) ceramics. However, the co-doped ceramic

shows a much higher T_c than the Sm-doped one, indicating better thermal stability (Supplementary Fig. 8). Compared with Sm-PMN-29PT (Sm = 2.5%), the Curie peak shifts to a higher temperature and sharpens due to La modifications and higher PT content. The Sm/La-PMN-PT (Sm = La = 0.75%) exhibits a low dielectric variation (14.7%) over the temperature range of 0–100 °C (Fig. 2h) and much improved thermal stability of the dielectric permittivity compared with other selected ceramics[34], which was also confirmed by the 15% change in the electric-field-induced strain in the same broad temperature range (Fig. 2i and Supplementary Fig. 9). To elucidate the phase transition state at various temperatures, temperature-dependent X-ray diffraction (XRD) was evaluated at temperatures from 0 to 100 °C (Supplementary Fig. 10). The sample exhibited mixed tetragonal (*P*4*mm*) and rhombohedral (*R*3*m*) phases according to the Rietveld refinement of the XRD data (Supplementary Fig. 11). The tetragonal *a* and *c* parameters showed slight changes with increasing temperature (Supplementary Fig. 12a). The tetragonal phase fraction (94%) and rhombohedral phase fraction (6%) remained almost constant in temperatures ranging between 0 and 100 °C (Supplementary Fig. 12b), demonstrating the notable thermal stability observed in Sm/La-PMN-PT (Sm = La = 0.75%) ceramics. Consequently, the electromechanical coupling factors (k_p, k_t and k_{33}) exhibited a minimal change (<5%) over the temperature range of 0–100 °C (Fig. 2j). In summary, the full matrix of dielectric, elastic and piezoelectric constants of 0.75%Sm/La-PMN-35PT ceramic was measured by the resonance technique and used to construct the complete property matrices (Supplementary Note 3 and Supplementary Table 4). As demonstrated in PMN-PT ceramics with a composition close to the morphotropic phase boundary, adding La can reduce the grain size and enhance the density[49]. The results indicate that the co-doped Sm/La-PMN-PT (Sm = La = 0.75%) ceramics (abbreviated as Sm/La-PMN-PT hereafter) possess a large piezoelectric coefficient (d_{33} = 1,000 pC N^{-1}), high dielectric permittivity (ε_r = 7,500), excellent electromechanical coupling factor (k_{33} = 0.77), high phase transition temperature (T_c = 150 °C) and high temperature stability. Thermal stability can guarantee less performance degradation during device processing, packaging and transportation, as well as broad temperature usage in different environments.

Design and performance of ultrasound arrays

The design of the 1D phased array is based on the traditional transducer three-port network[32] (Fig. 1g), including the active piezoelectric element, backing layer and two matching layers. The Sm/La-PMN-PT ceramic was chosen for phased-array transducer fabrication, whereas another commercially available piezoelectric material, namely, PZT-5H, was also selected (Baoding HongSheng Acoustics Electron Apparatus Co., Ltd, China) as a benchmark comparison (Supplementary Table 5). The suggested transducer frequency for bladder imaging from the literature is around 2–5 MHz (Supplementary Table 1). Supplementary Fig. 13 shows the geometry of the 1D phased array with the major components. The 1D phased array with 64 elements and a working frequency of 3.5 MHz is proposed to balance the spatial resolution and depth for bladder imaging. The corresponding ultrasound wavelength ($\lambda = c/f$, c = 1,540 m s^{-1} in water) in the soft tissue for 3.5 MHz is calculated as 440 µm. To meet the maximum half-wavelength requirement for the phased array to avoid side lobes[50], the pitch is selected as 220 µm and it equals the element width (170 µm) plus the kerf (50 µm). During the dicing process, the 30-µm-thick synthetic diamond blade achieved 50 µm space due to the vibration of the dicing blade. The aspect ratio of width/thickness is smaller than 1/3, which meets the requirement for desired thickness vibration[37]. The element length is selected as 14 mm (64 times the pitch) to obtain an acoustic beam with minimal spreading within the planned imaging depth. The flexible cable with the same electrode traces is aligned to the electrode on the array and placed between the elements and matching layer (Fig. 1i). The cross-section view shows that all the components have a uniform thickness and are firmly bonded by the epoxy solution under high-temperature pressure (Fig. 1j). Supplementary Note 4 and Supplementary Table 6 discuss the detailed simulation information and acoustic properties of each layer in the stack, and Supplementary Note 5 describes the fabrication process and characterization methods. Consistency of array performance is essential for high-quality ultrasonic imaging. The array's electrical impedance and acoustic performances were measured to investigate the uniformity of the array elements. The piezoelectric and acoustic performances of all the elements of both Sm/La-PMN-PT-based and PZT-5H-based arrays are shown in Fig. 3a–c and Supplementary Fig. 19. Supplementary Note 5 discusses the detailed simulation and experimental analyses. Clearly, the Sm/La-PMN-PT array not only has the better electromechanical properties (larger effective electromechanical coupling coefficient k_{eff} = 0.62) compared with the PZT array (k_{eff} = 0.52) but also has a higher bandwidth (12% improvement), suggesting that the Sm/La-PMN-PT array transducer has higher acoustic performance for ultrasonic imaging.

Ultrasound imaging on phantoms

To achieve real-time imaging, a data acquisition interface linked the array and cUSB-Patch with a Vantage 256 ultrasound system (Verasonics). Before performing human clinical trials, the fabricated arrays and cUSB-Patch were tested on three distinct phantoms to evaluate their acoustic performance and imaging capability. A phantom with fishing lines in a water tank was used to examine the resolution at various depths (Supplementary Fig. 25 and Methods). The simulation and experimental findings of the ultrasound point-spread function from a single array placed at the top of the wire targets are depicted in Supplementary Fig. 26 and described in Supplementary Note 6. Images are scaled with a 30 dB dynamic range from the brightest point in each image. The resolution is obtained from the measured 6 dB region, corresponding to the normalized curve's full-width at half-maximum. Comparing the simulation and experimental results (Supplementary Fig. 27) in both axial and lateral dimensions, the phased array demonstrated a relatively high degree of resolution. For instance, it could still achieve 0.6 mm of axial resolution at −18.2 cm and the same lateral resolution at −10.7 cm, which is suitable for imaging deep tissues and organs. However, the lateral resolution has a large difference between the experimental results and the simulation results at lower depth targets due to the split lobe. To resolve this issue, the strategy of multiple-phased-array design is proposed to keep similar lateral resolution during the increased depth.

To illustrate the FOV and resolution, an ultrasound phantom with a planar surface containing both wire and cylinder targets (model 040GSE, Computerized Imaging Reference Systems) was used. This phantom includes near-field targets, resolution targets, hyperechoic and hypoechoic targets, as well as other types of target (Supplementary Fig. 28). The commercial Verasonics C5-2v curved array probe, commonly used for imaging deep tissue, is used here as a point of reference (Fig. 3d,e). This figure shows that a single phased array has a larger FOV and similar imaging depth of ~14 cm compared with the C5-2v probe when not applying pressure and scanning across the 040GSE phantom (Fig. 3f,g and Supplementary Video 3), which is probably sufficient for bladder imaging in most people. The cUSB-Patch can offer a larger FOV (Fig. 3h) than the C5-2v probe and single array. Because the primary regions of interest scanned across all the transducers are the vertical/horizontal distance targets and axial/lateral resolution targets, each array acquired three typical images of the targeted areas and reconstructed a complete 2D image (Fig. 3h and Supplementary Fig. 29). The resolution of the vertical/horizontal distance targets are listed in Fig. 3i. It is clear that the axial resolution is less than 1.0 mm at both 40 cm and 90.0 mm depth and the minimum value is around 0.6 mm (Fig. 3j,k), which is close to the results obtained from the phantom with fishing lines. When we check the axial/lateral resolution targets at 3.0 cm depth (Fig. 3i(iii)) and 6.5 cm depth (Fig. 3i(iv)), the arrays

https://doi.org/10.1038/s41928-023-01068-x

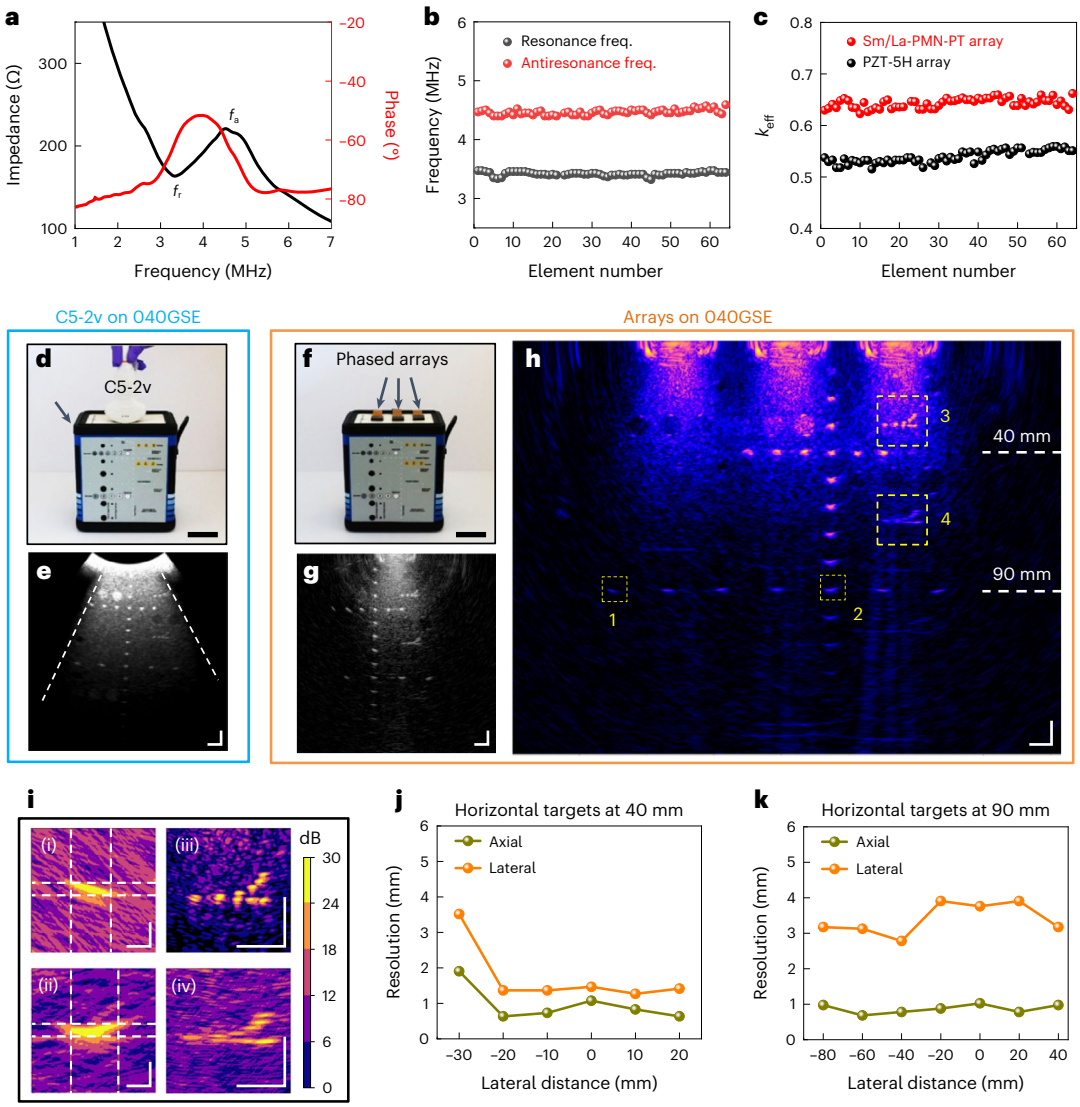

Fig. 3 | Piezoelectric and acoustic performances of phased-array transducers. **a**, Frequency dependence of the measured impedance and phase angle of the single element of the Sm/La-PMN-PT array. **b**, Resonance and antiresonance frequencies of 64 elements of the Sm/La-PMN-PT array. **c**, Comparison of k_{eff} of the Sm/La-PMN-PT array and PZT-5H array. **d**,**e**, Optical photograph (**d**) and image (**e**) of the C5-2v probe on the top surface of the planar phantom with ultrasound gel. **f**,**g**, Optical photograph (**f**) and image (**g**) from the single array on the top surface of the planar phantom with ultrasound gel. **h**, Reconstructed image from three arrays on the top surface of the planar phantom with ultrasound gel. **i**, Zoomed-in images from **h**: 1 and 2 are the lower horizontal targets and 3 and 4 are the axial/lateral resolution targets. **j**,**k**, Axial and lateral resolutions of the horizontal targets (distance between array, 5 cm): horizontal targets at 40 mm (**j**); horizontal targets at 90 mm (**k**). Scale bar, 5 cm (**d**, **f**), 1 cm (**e**, **g**, **h**), 2 mm (**i**).

separated targets with gaps as small as 0.5 mm in the axial direction and 2.0 mm in the lateral direction at 3.0 cm depth, and 0.5 mm in the axial direction and 3.0 mm in the lateral direction at 6.5 cm depth. If numerous arrays are positioned and aligned at measured intervals on the phantom, aggregated images of the entire phantom can be obtained (Supplementary Fig. 30). This was accomplished by sliding a single array across the surface in ~1 cm increments, followed by manual image registration (Supplementary Fig. 31). In addition, when we change the distance between arrays from 4 to 5 cm, there is no obvious difference in the imaging resolutions (Fig. 3j,k and Supplementary Fig. 32), which indicates that the patch can still maintain a similar image quality during short-distance stretchability.

Increasing the number of arrays expands the FOV and improves the wide-angle resolution, suggesting that the cUSB-Patch technology has a pathway to clinical utility for additional applications that require wide-FOV imaging. In addition, we examined different scan settings (with/without gel, an applied voltage) for practical applications, as gel greatly impacts daily usage and cleaning of the device, and a lower applied voltage is crucial for a portable device. When we replaced the ultrasound gel with a thin Ecoflex layer (180–200 μm) for acoustic coupling, the array produced images of comparable quality with those obtained using gel (Supplementary Fig. 33). Eliminating the requirement for the acoustic coupling gel will save time, reduce costs and improve accessibility of the technology. We varied the applied voltage from 5 to 50 V to compare the quality of the scan image (Supplementary Fig. 34). Targets at depths of 7 cm can still be observed at 5 V, demonstrating the potential applicability of this technology to the point-of-care setting, where energy efficiency and low-power requirements are key for successful clinical development.

To evaluate the imaging quality of cUSB-Patch on a curved surface, the US-18 fundamental ultrasound phantom (model US-18, Kyoto Kagaku) was used (Supplementary Fig. 35). We first evaluated the C5-2v probe using this phantom. With the C5-2v probe, achieving a broad FOV required applying a substantial amount of force (Supplementary Fig. 36)

https://doi.org/10.1038/s41928-023-01068-x

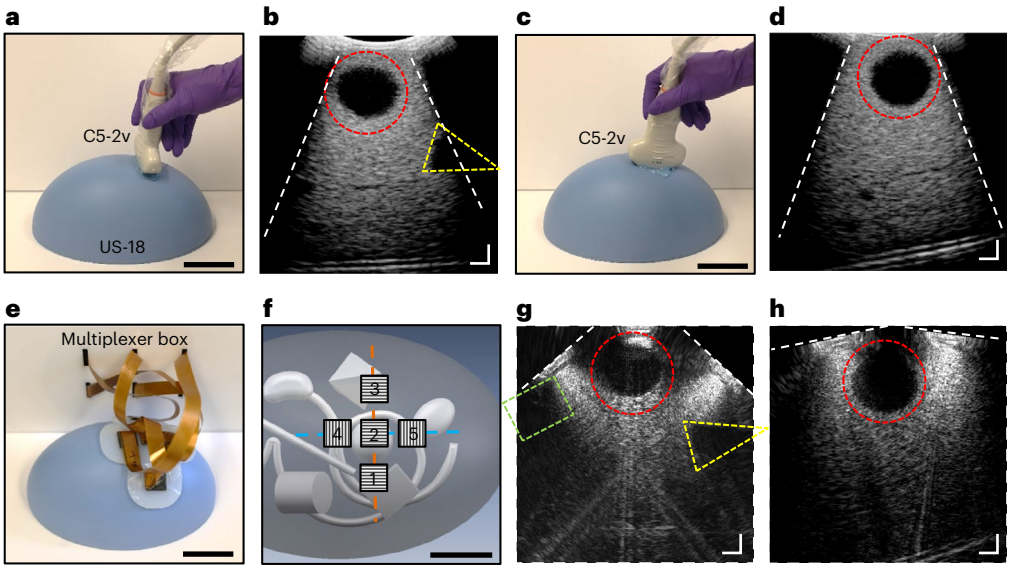

Fig. 4 | Real-time ultrasound imaging by the C5-2v commercial probe and the cUSB-Patch on the oval phantom. a,**b**, Optical photograph (**a**) and image (**b**) of the C5-2v probe on the top surface of the oval phantom with an ultrasound gel along the vertical direction. **c**,**d**, Optical photograph (**c**) and image (**d**) of the C5-2v probe on the top surface of the oval phantom with ultrasound gel along the horizontal direction. **e**, Optical photograph of the cUSB-Patch on the oval phantom. **f**, Schematic of the top view of the oval phantom and embedded 3D objects. The five black squares indicate the location of each array, and the black thin-line pattern in each black square indicates the orientation of 64 elements. The orange dashed line and blue dashed line indicate imaging along the vertical and horizontal orientations, respectively. **g**,**h**, The 2D reconstructed images on the oval phantom. The orange dashed line indicates the constructed image along the vertical orientation and the blue dashed line indicates the constructed image along the horizontal orientation, respectively. In all the ultrasound images, the white dashed lines indicate the FOV. The red dashed circle indicates the 2D view of the spherical object, the yellow dashed triangle indicates the 2D view of the tetragonal object and the green dashed rectangle indicates the 2D view of the rectangular object. The ultrasound gel was not applied to the US-18 fundamental ultrasound phantom for cUSB-Patch imaging. Scale bar, 5 cm (**a**, **c**, **e**, **f**), 1 cm (**b**, **d**, **g**, **h**).

and manual rotation of the probe to capture images in different orientations (Fig. 4a–d). When we used the cUSB-Patch to cover a partially curved surface (Fig. 4e), several three-dimensional (3D) objects were covered by the FOV of the patch (Fig. 4f and Supplementary Fig. 37). Five individual images can be simultaneously obtained to detect distinct 3D objects (Supplementary Fig. 38). The spherical object is visible in all the five images, whereas the tetragonal and rectangular objects are only visible in the left and right images, respectively. Arrays with mutual image planes were registered and combined, and the resulting larger images were orthogonally combined to produce a 3D image (Supplementary Fig. 39 and Supplementary Video 4). The 3D image rendering was performed using Napari, a Python library that provides capabilities for volumetric image visualization and graphics processing unit acceleration. Comparisons between the imaging operation of the C5-2v probe and cUSB-Patch demonstrate that the cUSB-Patch has several distinct advantages when imaging on curved surfaces, including operator independence (as the cUSB-Patch does not necessitate manually applied pressure or scanning), less image distortion and larger FOV by image reconstruction. The phantom data revealed that our phased arrays and cUSB-Patch are suitable for clinical studies on the human bladder.

Clinical real-time imaging of human urinary bladder

A human clinical study (Institutional Review Board (IRB) #2021P001706) was performed to evaluate the performance of cUSB-Patch, comparing the bladder volume estimation with a reference clinical system (GE LOGIQ E10 with the C1-6-D probe), and to assess the performance of each system with and without the use of ultrasound gel (Scan 11-08 Ultrasound Gel, Parker Laboratories). Human subjects ages 18–64 years were recruited with body mass index (BMI) ranging from 17 to 30 kg m^{-2}, and 60% of the subjects were women. The bladder was imaged when full, after partial voiding and after complete voiding. The full and partially empty bladder measurements are referred to as case I and case II, respectively, and were independently analysed. For each case, the imaging sequence was as follows: (1) C1-6-D probe without ultrasound gel, (2) cUSB-Patch without gel, (3) cUSB-Patch with gel and (4) C1-6-D probe with gel. The volume estimated by the conventional probe with gel was considered as the ground truth for error calculations. After the final measurement in each case, a wipe (Sani-Cloth AF3 Germicidal Disposable Wipe) was used to wipe away any gel residue on the subject and clean the surface of the cUSB-Patch. Methods and Supplementary Table 10 show the detailed scanning protocol.

Subjects A, B, C and D are shown as representative samples (Fig. 5 and Supplementary Figs. 42–63), comprising two males and two females within a BMI range of 18.19–27.98 kg m^{-2} and an age range of 24–45 years. The width (W), length (L) and height (H) of the bladder were measured in each case, and the volume was calculated according to the equation[51,52] $V = W \times L \times H \times 0.7$, matching the method used with the C1-6-D probe on LOGIQ E10. Supplementary Figs. 42–63 show the sonographic volume-estimating images from the C1-6-D probe and cUSB-Patch for four subjects and Supplementary Videos 5–8 show the representative videos for continuous monitoring on subject A. The statistical results for these subjects are shown in Fig. 5e–p. The mean volumes recorded with the cUSB-Patch without gel are greatly improved compared with the commercial C1-6-D probe without gel but comparable with its performance with gel. The statistical results for these subjects are shown in Fig. 6a,b. The LOGIQ E10 and C1-6-D probe produced images without gel in many cases by increasing the gain setting from 25 to 35 dB up to 90 dB. Nevertheless, the mean volume measurement error without gel was found to be −47.5 ± 34.9%. This was mainly due to a reduced FOV without gel, and in a few cases, no image could be obtained (treated as −100% error). When the cUSB-Patch was used with gel, the volume measurement was similar to the ground-truth

https://doi.org/10.1038/s41928-023-01068-x

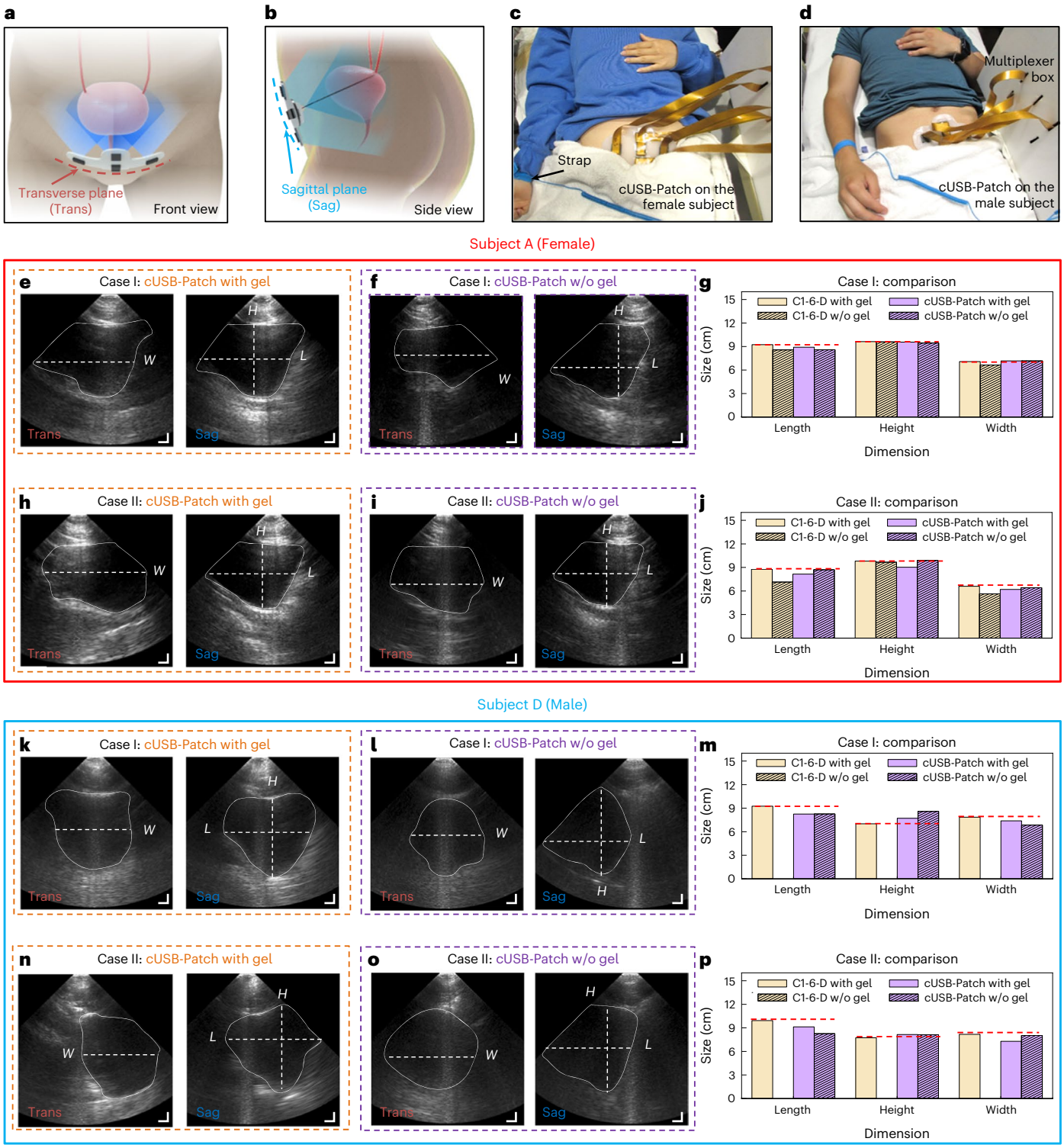

Fig. 5 | Real-time ultrasound imaging on the bladders of different subjects. **a**,**b**, Schematic of the working principle and FOV of the cUSB-Patch on the bladder. Three arrays collect images along the transverse plane (red dashed line), and two arrays collect images along the sagittal plane (blue dashed line). **c**,**d**, The cUSB-Patch, which is connected to the multiplexer box, was applied to the female (**c**) and male (**d**) subjects during the clinical study. **e**,**f**, Results on subject A (female). The ultrasound images of the full bladders for case I: the cUSB-Patch with gel (**e**) and without gel (**f**). **g**, Comparison of length, height and width of the bladder obtained by the C1-6-D probe and cUSB-Patch for subject A in case I. **h**,**i**, Ultrasound images of full bladders for case II: the cUSB-Patch with gel (**h**) and without gel (**i**). **j**, Comparison of length, height and width of the bladder obtained by the C1-6-D probe and cUSB-Patch for subject A in case II. **k**,**l**, Results for subject D (male). The ultrasound images of full bladders for case I: the cUSB-Patch with gel (**k**) and without gel (**l**). **m**, Comparison of length, height and width of the bladder obtained by the C1-6-D probe and cUSB-Patch for subject A in case I. **n**,**o**, Ultrasound images of full bladders for case II: the cUSB-Patch with gel (**n**) and without gel (**o**). **p**, Comparison of length, height and width of the bladder obtained by the C1-6-D probe and cUSB-Patch for subject A in case I. The depth of all the B-mode images is 15 cm. On all the B-mode images, the white solid closed loop shows the bladder wall, and the white dashed lines show the measurement of dimensions. The red dashed line in **g**, **j**, **m** and **p** indicates the value obtained from C1-6-D with gel as the baseline. Scale bar, 1 cm (**e**, **f**, **h**, **i**, **k**, **l**, **n**, **o**).

https://doi.org/10.1038/s41928-023-01068-x

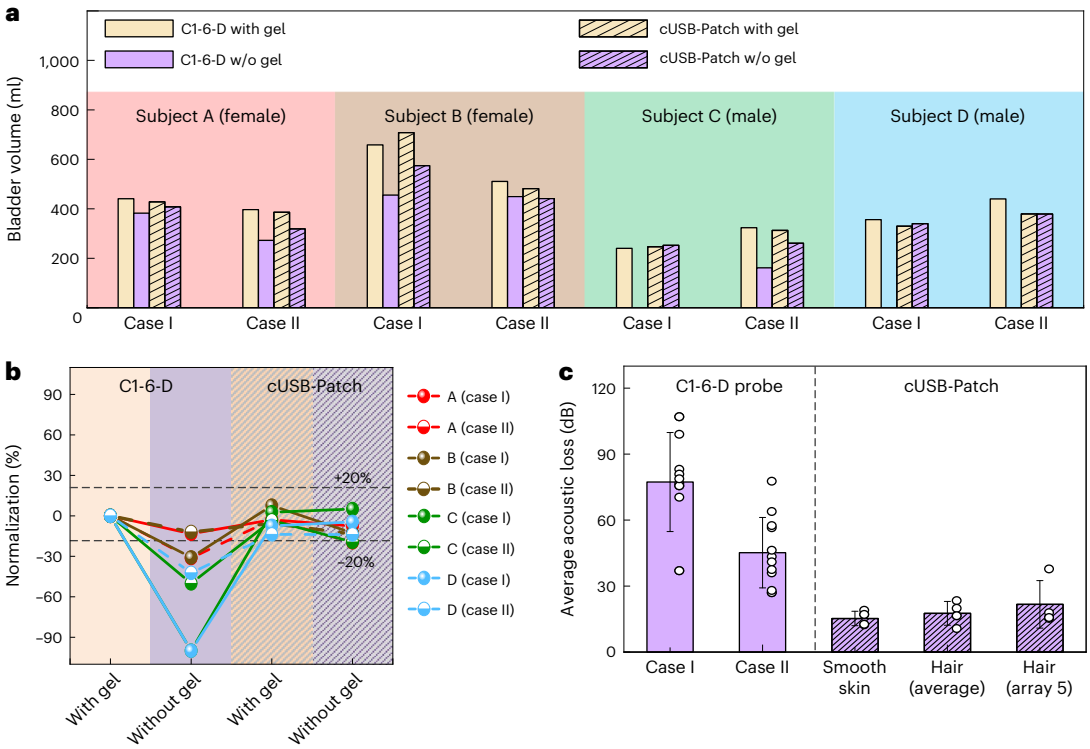

Fig. 6 | Summary and comparison of the calculated bladder volumes of four subjects. a, Comparison of the calculated bladder volumes. The volume was reported as zero when it could not be measured. There are eight tests for each subject, including C1-6-D probe with gel on a full bladder, C1-6-D probe without gel on a full bladder, C1-6-D probe with gel on a partially voided bladder, C1-6-D probe without gel on a partially voided bladder, cUSB-Patch with gel on a full bladder, cUSB-Patch without gel on a full bladder, cUSB-Patch with gel on a partially voided bladder and cUSB-Patch without gel on a partially voided bladder. **b**, Normalization of the calculated bladder volumes of four subjects in eight different tests. The volume of the C1-6-D probe with gel on the full bladder was used as the reference. **c**, Comparison of average acoustic loss in several no-gel imaging scenarios. The C1-6-D probe in case I shows the highest loss, followed by case II, which may be lower due to gel residue. For the cUSB-Patch, the lowest loss occurred for subjects with a smooth skin, followed by subjects with hair on their skin. Array 5 encountered the most hair due to being lowest on the abdomen and correspondingly shows the highest loss. The data are presented as mean values ± standard deviation (C1-6-D probe, $n = 12$ different areas; cUSB-Patch, $n = 5$). The circular dots show all the data points in each case.

value with a mean accuracy of −3.2 ± 6.4%. When used without gel, the cUSB-Patch demonstrated better performance than the C1-6-D probe without gel, achieving a mean accuracy of −10.8 ± 8.2%. This result is particularly notable because unlike the LOGIQ E10 system, the cUSB-Patch was used with a constant 40 dB gain setting, demonstrating the robustness and repeatability of the imaging without gel.

Another objective of the study was to evaluate and compare the acoustic coupling performance of the C1-6-D probe and cUSB-Patch with and without ultrasound gel on the skin. This was performed by taking the corresponding gel and no-gel images and measuring the change in image brightness (Methods). As shown in Fig. 6c and Supplementary Table 12, the acoustic loss was low when coupling to the flat-top phantom (<5 dB; Supplementary Fig. 31), moderate when coupling to a smooth skin surface (15.3 ± 7.2 dB) and slightly higher for individuals with a notable amount of abdominopelvic body hair (17.6 ± 10.0 dB). In particular, array 5 was the most probable to encounter pubic hair (21.7 ± 10.8 dB). In contrast, the acoustic loss in case I for the C1-6-D probe without gel was much higher at 77.3 ± 22.5 dB, whereas that for case II was 45.2 ± 16.0 dB. The difference between the loss values in cases I and II may indicate that a minute quantity of gel remained on the skin even after attempting removal.

Conclusions

We have reported a cUSB-Patch for non-invasive, real-time and continuous monitoring of soft tissues. Compared with clinical ultrasound probes, it shows a large FOV and is operator independent. The patch consists of multiple phased arrays of transducers that use a rare-earth-element-doped ceramic, namely, Sm/La-PMN-PT (Sm = La = 0.75%), with high dielectric and piezoelectric properties and a thermally stable range that make it suitable for the high frequencies used in clinical ultrasound imaging. These performance characteristics also make the ceramic promising for other electromechanical applications at room and elevated temperatures. The Sm/La-PMN-PT-ceramic-based phased array exhibited larger bandwidth compared with PZT-5H-based phased arrays, which improves the detection depth and resolution. Designing multiple arrays embedded in a soft substrate allowed imaging over a wide FOV and simultaneously on multiple axes, allowing full organ visibility without manual scanning or rotation by an operator.

The bladder patch, when used with ultrasound gel, measured a bladder volume in close agreement (error of −3.2 ± 6.4%) with the volume obtained using a clinical C1-6-D probe, indicating comparable image quality. It also demonstrated the capability to acquire ultrasound images without gel because the acoustic loss without gel was improved by approximately 60 dB compared with the C1-6-D probe. Without ultrasound gel, the C1-6-D probe showed a measurement error of −47.5%, whereas the cUSB-Patch had an error of −10.8%, comparable with the error with gel. In addition to precise bladder volume estimation, the cUSB-Patch was easily attached and detached multiple times during the clinical study and could be cleaned by a wipe (Supplementary Video 2).

Though the bladder was chosen as an illustrative example, the cUSB-Patch technology is suited for identifying and characterizing disease in any deep tissue, such as the liver and kidneys, via deep tissue

ultrasonography. In addition, the architecture of the cUSB-Patch can be adjusted to provide a FOV and scan depth suitable for shallower tissues (such as breast tissue)[45], enabling wearable ultrasound devices that can adapt to image tissue at multiple depths (Supplementary Fig. 64). Additional advantages of this system include reusability, high imaging performance without gel, operator independence without rotation and pressing, ease of cleaning and suitability for home-care settings.

Future studies will focus on several improvements. First, the simulation of mechanical deformation and acoustic performance of the adhesive layer will be investigated to meet the requirements of strong adhesion around the array–skin interface, robustness during mechanical stretching, lower attenuation and improved wave penetration for imaging. Second, the incorporation of 2D phased arrays would enable superior 3D imaging reconstructions to the 2D ultrasound images used here. Third, incorporating further post-processing steps such as coherence imaging, which uses adaptive weighting based on the cross-correlation between received signals to improve image contrast would enhance image quality, especially during long-term monitoring. Fourth, the addition of a portable data acquisition system with wireless data communication and energy-efficient machine learning inference would help further translate this technology into clinical use. Further development of the cUSB-Patch could allow wearable ultrasound devices to be deployable across a range of health-monitoring applications that require accurate, real-time and autonomous tissue monitoring.

Methods

Preparation of piezoelectric ceramics

$Pb_{(1-1.5y-1.5z)}Sm_yLa_z[(Mg_{1/3}Nb_{2/3})_{(1-x)}Ti_x]O_3$ (Sm/La-PMN-PT) with $x = 0.28–0.36$, $y = 0.005–0.010$ and $z = 0.005–0.010$ polycrystalline were prepared using a B-site-cation precursor method. The $MgNb_2O_6$ precursor materials were synthesized using Nb_2O_5 and $MgCO_3$ powders at an ambient temperature of 1,200 °C for 4 h. First, the powders were wet mixed using an alcohol solvent for 24 h by a zirconium ball milling process. Subsequently, the powder mixture was calcined at 850 °C for 2 h, followed by a binder-induced alcoholic vibratory milling process for 24 h. Next, the mixture was dried at 80 °C for 10 h and uniaxially pressed under 100 MPa to form fine thin pellets (thickness, 10 mm; diameter, 50 mm). A compaction step was introduced, which involved cold isostatic pressing under 100 MPa. Following compaction, the specimens were baked at 550 °C for 2 h and sintered at 1,200–1,250 °C for 2 h inside sealed corundum crucibles in an oxygenated atmosphere. Finally, in the presence of zirconia powders, the specimens were hot pressed at 900–1,100 °C for 2 h under 30 MPa inside a silicon carbide mould.

Characterization of piezoelectric ceramics

XRD (Bruker D8) was employed for determining the crystal structure and lattice parameters. The patterns were analysed using TOPAS-Academic software version 5.0 (Bruker AXS). The cross-sectional morphology and elemental energy-dispersive X-ray spectroscopy maps of the specimens were measured by a field-emission SEM instrument (Zeiss Gemini 500). For further electrical characterization, a silver paste was fired on both sides of the specimens at 600 °C for 10 min to form the electrodes. The specimens were poled in silicone oil at 25 °C for 10 min using a 30 kV cm^{-1} d.c. electric field. The piezoelectric coefficients were determined by a combination of impedance method and a quasi-static d_{33} meter. The resonance and antiresonance frequencies were measured using an HP 4194A impedance analyser. The temperature-dependent dielectric properties were determined using an LCR meter (HP 4284A) connected to a computer-controlled cooling–heating stage. According to the IEEE Standard on Piezoelectricity (176-1987), the temperature-dependent electromechanical coupling factors k_{33}, k_t and k_p were determined by the resonance method employing an impedance analyser (HP 4194A) connected to a computer-controlled cooling–heating stage. The unipolar strain induced by an external electric field was measured using a linear differential transducer driven by a lock-in amplifier (Stanford Research Systems, model SR830). Supplementary Note 3 discusses the method and characterization of the complete set of material constants for Sm/La-PMN-PT.

Fabrication and characterization of 1D array transducers

The whole device fabrication was achieved in the Center for Nanoscale Systems, Harvard University, and the YellowBox, Media Lab, Massachusetts Institute of Technology. The fabrication included four steps: (1) fabrication of a 1D array with 64 elements, (2) electrode deposition and patterning, (3) flexible cable bonding and (4) fabrication of matching and backing layers. The characterization of the 1D array included (1) frequency dependence of electrical impedance and (2) pulse-echo test for acoustic performance. Supplementary Note 5 with Supplementary Figs. 14–19 describe the detailed fabrication steps and characterization methods.

Fabrication of cUSB-Patch

Supplementary Fig. 3 shows the design and fabrication of the conformable substrate. First, the mould was fabricated by a 3D printer (Prusa i3 MK3S) and sanded to prevent the texture from the 3D printing process from creating an imprint on the patch. After cleaning the mould with isopropyl alcohol and deionized water, a thin layer of silicone rubber (Ecoflex 00-30, Smooth-On) was coated onto the mould by dip coating to achieve a thickness of 180–200 μm (smaller than the half-wavelength). Then, 50 g of Ecoflex (A and B) was mixed and poured into the mould (enough to fill the mould without overflowing). After curing for 4 h at room temperature, the Ecoflex substrate was carefully released from the mould. Then, the arrays were placed and embedded within their respective cavities and pressed to eliminate any air bubbles that might have been trapped between the silicone and matching layer. If air bubbles remain, it will diminish the overall acoustic energy delivered and cause bright artifacts in the acquired images. Finally, the additional Ecoflex was poured onto the backing layer to seal the gap between the arrays and substrate.

Data acquisition interface for single array and multiple arrays

Data acquisition was performed using the Vantage 256 ultrasound system, which provides an analogue front-end sufficient to simultaneously transmit and receive on up to 256 channels. To interface the fabricated transducers with the Vantage 256 system, an adaptable connector was designed and built to be compatible with a universal transducer adapter (UTA). Supplementary Fig. 21 describes the overall design and signal path from a transducer to the system. First, a Philips ATL C5-2v ultrasound transducer probe was deconstructed, which can support up to 128 individual elements. After detaching from the original printed circuit board (PCB), each individual signal line was checked by the multimeter to guarantee the connection to the corresponding pin in the UTA. It should be mentioned that the ordering of the UTA connector is not sequential and therefore does not follow the physical structure of a transducer. The order of the elements in the UTA connector was noted, and each cable was soldered onto PCB II accordingly. In PCB II, the final design grouped these cables into eight groups of 16 lines, took a sequential ordering at its inputs and rerouted the signals to match what the UTA connector would expect. To allow for the transducer to be interchangeable, PCB II interfaced via ribbon cables to the transducer's complementary PCB I. Due to each transducer consisting of 64 elements, two transducers could be connected in parallel with this interface.

For the cUSB-Patch with multiple arrays, each transducer array consists of 64 elements, and five arrays were used, making it necessary to develop an analogue multiplexer to expand the input/output capability of the Vantage 256 system. The multiplexer (Supplementary Fig. 22) provides the capability to interface the Vantage 256 system with up to eighteen 128-channel arrays, for a total capacity of 2,304 channels

(256 simultaneously). Each array is connected to a multiplexer card (Supplementary Fig. 23a), which contains 128 high-voltage analogue single-pole/single-throw switches. The multiplexer card plugs into a backplane, which wires all the corresponding analogue channels in parallel. In normal operation, one multiplexer card will enable all its switches and connect to the backplane analogue bus, whereas all the other multiplexer cards on the bus are disabled. The Vantage 256 system connects to a pickoff card (Supplementary Fig. 23b), plugging into the backplane to access the analogue bus. The analogue signals travel on ribbon cables from the pickoff card to an adaptor card that provides the conversion to the native Vantage 256-compatible cable. The multiplexer is designed to support computer control, providing external digital interfaces including Inter-Integrated Circuit (I2C) and a high-speed serial peripheral interface (SPI) transmitted using low voltage differential signaling (LVDS). Each multiplexer card contains a microcontroller and obtains a unique address according to which slot it is plugged into on the backplane. For convenience, an Arduino Due board was used to implement a USB-to-I2C bridge, allowing a personal computer to control the multiplexer using serial commands. It should be noted that we did not perform any electrical impedance matching on the array with the Verasonics system. The transducer impedance was approximately 200 Ω, and the Verasonics internal impedance matching was set to 250 Ω.

The imaging acquisition system includes (1) a Vantage 256 system with a UTA, (2) a multiplexer switch box with an array-to-system connection card, (3) multiple arrays of the cUSB-Patch, (4) blue-coloured electrostatic discharge wrist straps for both operator and subjects to protect the system electronics from static electricity, (5) a monitor to display the software and images, (6) a power cable for the switch and (7) a USB cable for communication (Supplementary Fig. 24). The whole system and cUSB-Patch passed the electrical inspection by the biomedical engineering team at Massachusetts General Hospital (no. 40200450). Arrays were connected to the Vantage 256 system using the custom UTA connector and were driven with a single-cycle sine pulse at 50 V with a 3.5 MHz centre frequency. During image acquisition, a phased-array beamformer was used to obtain a real-time image to visually align the transducer over the desired region on the phantom. After alignment was completed, a synthetic array transmit/receive sequence was used, and the raw received data were stored and beamformed in post-processing.

Acoustic imaging on different phantoms

The acoustic performance of the single array was initially evaluated using a wire phantom consisting of two parallel stable plates and eight fishing lines with a diameter of 0.2 mm (around the half-wavelength) (Supplementary Fig. 25). All the fishing lines were submerged in deionized water in the tank with a one-inch line-to-line spacing. A three-axis stage (DTS50, Thorlabs) was used to adjust the height and position of the array. During the test, the array was submerged in deionized water and positioned at three different locations to collect the ultrasound images of fishing lines using Vantage 256. Then, the multipurpose, multitissue ultrasound phantom (model 040GSE Computerized Imaging Reference Systems) was used for performance and quality assurance testing of the phased array. For this phantom, the gel was used to ensure the acoustic coupling (Aquasonic 100 Ultrasound Transmission Gel, Parker Laboratories). The US-18 fundamental ultrasound phantom (Kyoto Kagaku) with an oval shape and a curved surface was used for the cUSB-Patch imaging without the use of gel. The C5-2v convex ultrasound probe (Verasonics) was also used for comparison.

Biologic safety study

Before the clinical study, the spatial peak temporal average intensity (I_{SPTA}), the spatial peak pulse average intensity (I_{SPPA}) and the mechanical index (MI) were quantified to assess the biologic safety (Supplementary Note 7). The acoustic pressure generated by the entire phased array was measured inside a ten-gallon water tank filled with degassed water. The transducer was fixed to the side of the tank using double-sided tape and was driven by the Vantage 256 system. The previously described hydrophone was mounted on a three-axis motion stage (DTS50, Thorlabs) used to measure the acoustic pressure. The hydrophone's generated voltage is fed through a preamplifier (Onda AG-2010 Hydrophone Preamplifier), which is then read and captured using an oscilloscope (Tektronix 3 Series MDO32). Finally, a trigger signal was also output from the Vantage 256 system into the oscilloscope to facilitate data capture.

The measured results (I_{SPTA} = 0.08 mW cm^{-2}, I_{SPPA} = 10.10 W cm^{-2} and MI = 0.27) below the FDA's acoustic output limits (I_{SPTA} = 0.72 mW cm^{-2}, I_{SPPA} = 190.00 W cm^{-2} and MI = 1.90) for ultrasound diagnosis (Supplementary Fig. 40). To assess tissue heating, a piece of bovine tissue was used to mimic human tissue and was imaged using five arrays positioned on the tissue surface with converging focal regions to achieve the maximum temperature rise at a single point. After 30 min of continuous operation, the temperature difference between the focused point and another area in the meat was negligible (~0.3 °C) (Supplementary Fig. 41), consistent with the measured very low thermal index (2.7×10^{-3}) implied by the output levels (Supplementary Note 8). These experiments indicate that the cUSB-Patch is unlikely to cause any harmful bioeffects due to acoustic power or heat generation.

In vivo clinical study

The Mass General Brigham IRB (#2021P001706) approved the prospective pilot study of twenty subjects and served as the central IRB for the study. Written informed consent was obtained from each subject before initiating the study procedures. All the procedures were performed in accordance with the Health Insurance Portability and Accountability Act and the Declaration of Helsinki.

Inclusion criteria were age of 18–65 years and BMI between 17 and 30 kg m^{-2}. Subjects were excluded for confirmed or suspected pregnancy; presence of an implanted electronic device; history of bladder outlet obstruction, urinary retention or benign prostatic hyperplasia; history of bladder, prostate or urethral surgery; and the presence of an indwelling urinary catheter. We recruited 20 subjects with a BMI between 18.19 and 27.98 kg m^{-2}. Subjects were requested to arrive with a full bladder before the start of imaging. Imaging was performed using a clinical GE LOGIQ E10 system (GE Healthcare) with a curvilinear transducer (GE C1-6-D curved array probe, 192 elements; FOV, 70°) and the Vantage 256 system with the custom conformable transducer (cUSB-Patch). Scan 11-08 Ultrasound Gel (Parker Laboratories) was used for acoustic coupling. The two operators from Mass General Hospital included an ultrasound radiologist with 15 years of experience and a sonographer with 12 years of experience. Both completed hands-on training with the cUSB-Patch and demonstrated proficiency with the GE LOGIQ E10 device before clinical trials.

The initial 11 subjects were utilized for the technical optimization of the bladder patch performance in humans, including optimization of the transmit–receive pulse sequences, procedures and data-recording methods. The following four consecutive patients were analysed for the purposes of proof of concept. Subjects were asked to lay supine on an examination table and adjust their clothing for ultrasound scanning access to the lower abdomen. Each scanning sequence began without the utilization of the acoustic coupling gel. First, the C1-6-D probe was used without gel to acquire sweep images in the transverse and sagittal planes. Additional sagittal and transverse still images were acquired to maximize the bladder size within the image for use in computing the bladder volume. Next, both subject and clinician wore antistatic wrist bands (Croing) to protect the electronics from electrostatic discharge. The cUSB-Patch was placed on the subject's lower abdomen and positioned above the bladder using the central transducer element to guide placement with the long axis aligned with the transverse plane of the body. Each array was connected to the Vantage 256

machine by switching the multiplexer, and several seconds of video were acquired using a focused beamformer. The synthetic array data were then acquired and saved (Supplementary Note 7). Gel was then applied to the abdomen, and the same procedures were performed with the cUSB-Patch first, followed by the C1-6-D probe. On the completion of imaging, gel was removed from the skin with a wipe (Sani-Cloth AF3 Germicidal Disposable Wipe). Each subject was asked to partially void and later entirely void their bladders, and the voided volumes were recorded. Imaging was repeated after voiding each time. As a result, data acquisitions were performed on full, partial and empty bladder volumes for each subject. The patch was disinfected between subjects using another wipe.

Measurement and calculation of the bladder volume were performed using the standard clinical method of manually selecting high-quality images from each acquisition[51,52], visually identifying the bladder walls, and measuring each of the width, length and height values at their widest points (Fig. 5e–p). The bladder volume was estimated as $V = W \times L \times H \times 0.7$. The same measurement and calculation methods were used for the images from the C1-6-D probe and cUSB-Patch. The images from C1-6-D with gel were treated as the ground truth for all the volume error calculations. The mean and standard deviations of the volume error were reported for several cases of interest: C1-6-D probe without gel, cUSB-Patch with gel and cUSB-Patch without gel (Supplementary Table 11).

The acoustic loss was also measured to determine the performance of different acoustic coupling media. The measurement was performed by comparing image brightness between the corresponding gel and no-gel images, as well as considering any changes in the system gain. The acoustic loss was determined using a successive approximation algorithm, where the gel image brightness was iteratively scaled and thresholded according to the image dynamic range to match the mean values of the images (in this case, 'mean' refers to the mean value of the non-thresholded pixels, that is, pixels that are not black). An iterative approach was used because of the non-Gaussian statistical distribution of pixel brightness and the nonlinear behaviour of thresholding.

Reporting summary

Further information on research design is available in the Nature Portfolio Reporting Summary linked to this article.

Data availability

The raw data from human trials are available from the corresponding author, subject to approval from The Mass General Brigham IRB (#2021P001706). All other data that support the findings of this study are available from the corresponding author upon reasonable request.

Code availability

The codes based on Python used for the synthetic array beamforming, simulation and image analysis are available from the corresponding author on reasonable request.

References

1. Dagdeviren, C. et al. Recent progress in flexible and stretchable piezoelectric devices for mechanical energy harvesting, sensing and actuation. *Extrem. Mech. Lett.* **9**, 269–281 (2016).
2. Wang, C., Wang, C., Huang, Z. & Xu, S. Materials and structures toward soft electronics. *Adv. Mater.* **30**, 1801368 (2018).
3. Fernandez, S. V. et al. On-body piezoelectric energy harvesters through innovative designs and conformable structures. *ACS Biomater. Sci. Eng.* **9**, 2070–2086 (2021).
4. Dagdeviren, C., Li, Z. & Wang, Z. L. Energy harvesting from the animal/human body for self-powered electronics. *Annu. Rev. Biomed. Eng.* **19**, 85–108 (2017).
5. Fernandez, S. V. et al. Ubiquitous conformable systems for imperceptible computing. *Foresight* **24**, 75–98 (2022).
6. Dagdeviren, C. et al. Conformal piezoelectric systems for clinical and experimental characterization of soft tissue biomechanics. *Nat. Mater.* **14**, 728–736 (2015).
7. Guan, Y. et al. Soft, super-elastic, all-polymer piezoelectric elastomer for artificial electronic skin. *ACS Appl. Mater. Interfaces* **15**, 1736–1747 (2023).
8. Dagdeviren, C. et al. Conformal piezoelectric energy harvesting and storage from motions of the heart, lung, and diaphragm. *Proc. Natl Acad. Sci. USA* **111**, 1927–1932 (2014).
9. Nayeem, M. O. G. et al. All-nanofiber–based, ultrasensitive, gas-permeable mechanoacoustic sensors for continuous long-term heart monitoring. *Proc. Natl Acad. Sci. USA* **117**, 7063–7070 (2020).
10. Sun, T. et al. Decoding of facial strains via conformable piezoelectric interfaces. *Nat. Biomed. Eng.* **4**, 954–972 (2020).
11. Amiri, N., Tasnim, F., Tavakkoli Anbarani, M., Dagdeviren, C. & Karami, M. A. Experimentally verified finite element modeling and analysis of a conformable piezoelectric sensor. *Smart Mater. Struct.* **30**, 085017 (2021).
12. Dagdeviren, C. et al. Flexible piezoelectric devices for gastrointestinal motility sensing. *Nat. Biomed. Eng.* **1**, 807–817 (2017).
13. Chun, S. et al. An artificial neural tactile sensing system. *Nat. Electron.* **4**, 429–438 (2021).
14. Dagdeviren, C. et al. Conformable amplified lead zirconate titanate sensors with enhanced piezoelectric response for cutaneous pressure monitoring. *Nat. Commun.* **5**, 4496 (2014).
15. Wang, C. et al. Monitoring of the central blood pressure waveform via a conformal ultrasonic device. *Nat. Biomed. Eng.* **2**, 687–695 (2018).
16. Wang, F. et al. Flexible Doppler ultrasound device for the monitoring of blood flow velocity. *Sci. Adv.* **7**, eabi9283 (2021).
17. Kim, T. et al. Flexible 1–3 composite ultrasound transducers with silver nanowire-based stretchable electrodes. *IEEE Trans. Ind. Electron.* **67**, 6955–6962 (2019).
18. Pashaei, V. et al. Flexible body-conformal ultrasound patches for image-guided neuromodulation. *IEEE Trans. Biomed. Circuits Syst.* **14**, 305–318 (2020).
19. Sadeghpour, S., Lips, B., Kraft, M. & Puers, R. Bendable piezoelectric micromachined ultrasound transducer (PMUT) arrays based on silicon-on-insulator (SOI) technology. *J. Microelectromech. Syst.* **29**, 378–386 (2020).
20. Wang, C. et al. Continuous monitoring of deep-tissue haemodynamics with stretchable ultrasonic phased arrays. *Nat. Biomed. Eng.* **5**, 749–758 (2021).
21. Liu, W., Chen, W., Zhu, C. & Wu, D. Design and micromachining of a stretchable two-dimensional ultrasonic array. *Micro Nano Eng.* **13**, 100096 (2021).
22. Zhang, Q. et al. Transformable ultrasonic array transducer for multiscale imaging and beamforming. *IEEE Trans. Ind. Electron.* **69**, 3078–3087 (2022).
23. Wang, C. et al. Bioadhesive ultrasound for long-term continuous imaging of diverse organs. *Science* **377**, 517–523 (2022).
24. Yu, C.-C. et al. A conformable ultrasound patch for cavitation-enhanced transdermal cosmeceutical delivery. *Adv. Mater.* **35**, 2300066 (2023).
25. de Oliveira, T. F., Pai, C. N., Matuda, M. Y., Adamowski, J. C. & Buiochi, F. Development of a 2.25 MHz flexible array ultrasonic transducer. *Res. Biomed. Eng.* **35**, 27–37 (2019).
26. Du, W. et al. Conformable ultrasound breast patch for deep tissue scanning and imaging. *Sci. Adv.* **9**, eadh5325 (2023).
27. Hu, H. et al. A wearable cardiac ultrasound imager. *Nature* **613**, 667–675 (2023).
28. Hu, H. et al. Stretchable ultrasonic transducer arrays for three-dimensional imaging on complex surfaces. *Sci. Adv.* **4**, eaar3979 (2018).

29. Yang, Y. et al. A flexible piezoelectric micromachined ultrasound transducer. *RSC Adv.* **3**, 24900–24905 (2013).
30. Zhu, Q. et al. A piezoelectric micro-machined ultrasonic transducer array based on flexible substrate. In *Proc. 13th Annual IEEE International Conference on Nano/Micro Engineered and Molecular Systems* 345–348 (IEEE, 2018).
31. Wang, Z. et al. A flexible ultrasound transducer array with micro-machined bulk PZT. *Sensors* **15**, 2538–2547 (2015).
32. Zhou, Q., Lam, K. H., Zheng, H., Qiu, W. & Shung, K. K. Piezoelectric single crystal ultrasonic transducers for biomedical applications. *Prog. Mater. Sci.* **66**, 87–111 (2014).
33. Li, C. et al. Atomic-scale origin of ultrahigh piezoelectricity in samarium-doped PMN-PT ceramics. *Phys. Rev. B* **101**, 140102 (2020).
34. Li, F. et al. Ultrahigh piezoelectricity in ferroelectric ceramics by design. *Nat. Mater.* **17**, 349–354 (2018).
35. Zhou, S., Lin, D., Su, Y., Zhang, L. & Liu, W. Enhanced dielectric, ferroelectric, and optical properties in rare earth elements doped PMN-PT thin films. *J. Adv. Ceram.* **10**, 98–107 (2021).
36. Zhang, Z. et al. New Sm-PMN-PT ceramic-based 2-D array for low-intensity ultrasound therapy application. *IEEE Trans. Ultrason. Ferroelectr. Freq. Control* **67**, 2085–2094 (2020).
37. Zhang, Z. et al. High-performance ultrasound needle transducer based on modified PMN-PT ceramic with ultrahigh clamped dielectric permittivity. *IEEE Trans. Ultrason. Ferroelectr. Freq. Control* **65**, 223–230 (2018).
38. Kristiansen, N. K., Djurhuus, J. C. & Nygaard, H. Design and evaluation of an ultrasound-based bladder volume monitor. *Med. Biol. Eng. Comput.* **42**, 762–769 (2004).
39. Tanaka, R. & Abe, T. Measurement of the bladder volume with a limited number of ultrasonic transducers. In *2010 IEEE International Ultrasonics Symposium* 1783–1786 (IEEE, 2010).
40. van Leuteren, P. G. et al. URIKA, continuous ultrasound monitoring for the detection of a full bladder in children with dysfunctional voiding: a feasibility study. *Biomed. Phys. Eng. Express* **3**, 017005 (2017).
41. Kuru, K. et al. Intelligent autonomous treatment of bedwetting using non-invasive wearable advanced mechatronics systems and MEMS sensors. *Med. Biol. Eng. Comput.* **58**, 943–965 (2020).
42. Kuru, K., Ansell, D., Jones, M., De Goede, C. & Leather, P. Feasibility study of intelligent autonomous determination of the bladder voiding need to treat bedwetting using ultrasound and smartphone ML techniques. *Med. Biol. Eng. Comput.* **57**, 1079–1097 (2019).
43. Fournelle, M. et al. Portable ultrasound research system for use in automated bladder monitoring with machine-learning-based segmentation. *Sensors* **21**, 6481 (2021).
44. Jo, H. G. et al. Forward-looking ultrasound wearable scanner system for estimation of urinary bladder volume. *Sensors* **21**, 5445 (2021).
45. Dagdeviren, C. & Zhang, L. Methods and apparatus for imaging with conformable ultrasound patch. US patent 16/658,237 (2020).
46. Yang, J. C. et al. Geometrically engineered rigid island array for stretchable electronics capable of withstanding various deformation modes. *Sci. Adv.* **8**, eabn3863 (2023).
47. Fielding, J. T., Shrout, T. R. & Jang, S. J. Increased operating temperature range in La-modified $Pb(Mg_{1/3}Nb_{2/3})O_3$-$PbTiO_3$ relaxor ferroelectric-based transducers. In *Proc. 1994 IEEE International Symposium on Applications of Ferroelectrics* 158–161 (IEEE, 1994).
48. Choi, S. W., Shrout, T. R., Jang, S. J. & Bhalla, A. S. Morphotropic phase boundary in Pb $(Mg_{13}Nb_{23})$ O_3-$PbTiO_3$ system. *Mater. Lett.* **8**, 253–255 (1989).
49. Kim, N., Jang, S. J. & Shrout, T. R. Relaxor based fine grain piezoelectric materials. In *Proc. 1990 IEEE 7th International Symposium on Applications of Ferroelectrics* 605–609 (IEEE, 1990).
50. Jiang, X.-J. et al. A microscale linear phased-array ultrasonic transducer based on PZT ceramics. *Sensors* **19**, 1244 (2019).
51. Bala, K. G. & Chou, Y.-H. Ultrasonography of the urinary bladder. *J. Med. Ultrasound* **18**, 105–114 (2010).
52. Bih, L.-I., Ho, C.-C., Tsai, S.-J., Lai, Y.-C. & Chow, W. Bladder shape impact on the accuracy of ultrasonic estimation of bladder volume. *Arch. Phys. Med. Rehab.* **79**, 1553–1556 (1998).

Acknowledgements

C.D. thanks C. Dagdeviren and H. E. Dagdeviren for fruitful discussions throughout this project. This work was supported by the National Science Foundation CAREER: Conformable Piezoelectrics for Soft Tissue Imaging (grant no. 2044688), 3M Non-Tenured Faculty Award, Sagol Weizmann-MIT Bridge Program, Texas Instruments Inc. and MIT Media Lab Consortium funding. W.D. was supported by the National Science Foundation Graduate Research Fellowship Program (grant no. 2141064). Any opinions, findings and conclusions or recommendations expressed in this material are those of the author(s) and do not necessarily reflect the views of the National Science Foundation. T.T.P. was supported by the 2020 ARRS Scholar Award. This work was performed in part at the Harvard University Center for Nanoscale Systems (CNS)—a member of the National Nanotechnology Coordinated Infrastructure Network (NNCI), which is supported by the National Science Foundation under NSF award no. ECCS-2025158. We thank P. Cao and C. Peng for technical discussions; H. Park and J. Tresback for assistance on microfabrication; O. Drori, A. Mamistvalov, K. Brahma and A. Benjamin for imaging discussion; E. Suh for patch design discussion; and M.-C. O'Connell, M. Martin, E. Sands and Y. Gu for assisting on the clinical study.

Author contributions

C.D. conceived the research idea, designed the research direction and directed all the research activities. A.E.S. directed the proposed implementation of the technology and supervised the clinical study. A.P.C. contributed to the overall system architecture. L.Z. and C.D. conceived the research methodology and aims. L.Z., C.M. and C.D. designed the experiments. D.L. processed and characterized the piezoelectric ceramics. W.L. supervised the materials investigation. D.L. and L.J. studied the structure and morphology of ceramics. D.L., L.Z. and F.L. analysed the performance of the ceramics. C.D., L.Z. and D.M. designed the patch for the bladder. L.Z. designed and fabricated the ultrasound arrays. D.M. and L.Z. characterized the array and fabricated the patch. C.M. and D.M. designed the electronic circuits for data acquisition. S.J.S., assisted by V.K., conducted the coding and ultrasound signal processing for image generation by the Verasonics Vantage 256 system. L.Z., C.M., S.J.S. and D.M. conducted the in vitro ultrasound imaging. I.I.S., W.D. and S.V.F. assisted with the device characterization. V.K. coordinated the in vitro study at Mass General Hospital, and T.T.P. coordinated the in vivo study, including overseeing recruitment and scheduling (with H.E.), obtaining subject informed consent and monitoring subject safety. H.E. recruited the subjects and assisted in the clinical study. L.Z., D.M., S.J.S. and V.K. conducted the safety testing and prepared the related IRB document filings. D.H., T.T.P., L.Z. and C.M. designed the clinical-trial imaging protocols. D.H. and Q.L. performed the image acquisition of the human subject. C.M., S.J.S., T.T.P., H.E., V.K., D.H. and Q.L. executed the in vivo study and analysed the data. Y.C.E. assisted in the imaging process. W.D. and D.S. composed the layout of Supplementary Videos 1–8 and formed the videos. All authors contributed to the manuscript writing.

Competing interests
A.P.C. is on the Board of Analog Devices. The other authors declare no competing interests.

Additional information
Supplementary information The online version contains supplementary material available at https://doi.org/10.1038/s41928-023-01068-x.

Correspondence and requests for materials should be addressed to Canan Dagdeviren.

Peer review information *Nature Electronics* thanks Yangzhi Zhu, Qifa Zhou and the other, anonymous, reviewer(s) for their contribution to the peer review of this work.

nature portfolio

Corresponding author(s): Canan Dagdeviren

Last updated by author(s): Sep 1, 2023

Reporting Summary

Nature Portfolio wishes to improve the reproducibility of the work that we publish. This form provides structure for consistency and transparency in reporting. For further information on Nature Portfolio policies, see our Editorial Policies and the Editorial Policy Checklist.

Statistics

For all statistical analyses, confirm that the following items are present in the figure legend, table legend, main text, or Methods section.

n/a	Confirmed	
☐	☒	The exact sample size (*n*) for each experimental group/condition, given as a discrete number and unit of measurement
☐	☒	A statement on whether measurements were taken from distinct samples or whether the same sample was measured repeatedly
☒	☐	The statistical test(s) used AND whether they are one- or two-sided *Only common tests should be described solely by name; describe more complex techniques in the Methods section.*
☒	☐	A description of all covariates tested
☒	☐	A description of any assumptions or corrections, such as tests of normality and adjustment for multiple comparisons
☐	☒	A full description of the statistical parameters including central tendency (e.g. means) or other basic estimates (e.g. regression coefficient) AND variation (e.g. standard deviation) or associated estimates of uncertainty (e.g. confidence intervals)
☒	☐	For null hypothesis testing, the test statistic (e.g. *F*, *t*, *r*) with confidence intervals, effect sizes, degrees of freedom and *P* value noted *Give P values as exact values whenever suitable.*
☒	☐	For Bayesian analysis, information on the choice of priors and Markov chain Monte Carlo settings
☒	☐	For hierarchical and complex designs, identification of the appropriate level for tests and full reporting of outcomes
☒	☐	Estimates of effect sizes (e.g. Cohen's *d*, Pearson's *r*), indicating how they were calculated

Our web collection on statistics for biologists contains articles on many of the points above.

Software and code

Policy information about availability of computer code

Data collection	Data collection of the ultrasound signal was carried out with the Verasonics Vantage platform.
Data analysis	All data collected during in vitro and in vivo analysis was analyzed and plotted in OriginPro 2018 64-bit software. The KLM modeling was conducted in the PiezoCAD software (Pro. 4.0.1). The custom codes based on Python 3.8 were used for SAR beamforming, simulation, and image analysis.

For manuscripts utilizing custom algorithms or software that are central to the research but not yet described in published literature, software must be made available to editors and reviewers. We strongly encourage code deposition in a community repository (e.g. GitHub). See the Nature Portfolio guidelines for submitting code & software for further information.

Data

Policy information about availability of data

All manuscripts must include a data availability statement. This statement should provide the following information, where applicable:

- Accession codes, unique identifiers, or web links for publicly available datasets
- A description of any restrictions on data availability
- For clinical datasets or third party data, please ensure that the statement adheres to our policy

The data supporting the results in this study are available within the paper and its Supplementary Information. The raw data from human trials are available from the corresponding author, subject to approval from The Mass General Brigham Institutional Review Board (IRB) (#2021P001706).

Human research participants

Policy information about studies involving human research participants and Sex and Gender in Research.

Reporting on sex and gender	Subjects were recruited to ensure adequate representation of morphologic features unique to each gender. Individuals will not be excluded from the proposed research study on the basis of gender.
Population characteristics	We recruited 20 subjects with the age between 18-65 years and BMI between 18.19-27.98 kg/m2. The data of four subjects were studied in this manuscript. Healthy Subject A, Female, age 24, BMI: 22.67 kg/m2, no relevant health conditions. Healthy Subject B, Female, age 32, BMI: 18.19 kg/m2, no relevant health conditions. Healthy Subject C, Male, age 45, BMI: 24.78 kg/m2, no relevant health conditions. Healthy Subject D, Male, age 25, BMI: 27.98 kg/m2, no relevant health conditions.
Recruitment	We used Rally (https://rally.partner.org/) to recruit subjects. Healthy subjects were recruited to represent a variety of ages, genders and cultural backgrounds. There is no self-selection or other bias.
Ethics oversight	All procedures in the in vivo trials were performed in accordance with the experimental protocol approved by the Mass General Brigham Institutional Review Board (IRB) (#2021P001706). The participants gave informed consent.

Note that full information on the approval of the study protocol must also be provided in the manuscript.

Field-specific reporting

Please select the one below that is the best fit for your research. If you are not sure, read the appropriate sections before making your selection.

☒ Life sciences ☐ Behavioural & social sciences ☐ Ecological, evolutionary & environmental sciences

For a reference copy of the document with all sections, see nature.com/documents/nr-reporting-summary-flat.pdf

Life sciences study design

All studies must disclose on these points even when the disclosure is negative.

Sample size	5 arrays with closed performance were selected from 10 arrays to make the cUSB-Patch. One patch with 5 arrays was used to perform in vivo tests on four subjects.
Data exclusions	No data were excluded.
Replication	All attempts at replication were successful. For each subject and each case, the patch imaged bladder for several minutes using all five arrays to achieve multiple images. The same patch was used for four subjects in different, scheduled times and dates.
Randomization	One type of device was tested following same protocol for in vivo trial, but we tried to collect wide variety of subjects.
Blinding	Data collection and analysis for each subject were performed by different researchers.

Reporting for specific materials, systems and methods

We require information from authors about some types of materials, experimental systems and methods used in many studies. Here, indicate whether each material, system or method listed is relevant to your study. If you are not sure if a list item applies to your research, read the appropriate section before selecting a response.

Materials & experimental systems

n/a	Involved in the study
☒	☐ Antibodies
☒	☐ Eukaryotic cell lines
☒	☐ Palaeontology and archaeology
☒	☐ Animals and other organisms
☒	☐ Clinical data
☒	☐ Dual use research of concern

Methods

n/a	Involved in the study
☒	☐ ChIP-seq
☒	☐ Flow cytometry
☒	☐ MRI-based neuroimaging